

Metal-Free Nitrogen- and Boron-Codoped Mesoporous Carbons for Primary Amides Synthesis from Primary Alcohols via Direct Oxidative Dehydrogenation

Sensen Shang,^{†,⊥} Pei-Pei Chen,^{‡,§,⊥} Lianyue Wang,[†] Ying Lv,[†] Wei-Xue Li,^{*,‡,||} and Shuang Gao^{*,†}

[†]Dalian National Laboratory for Clean Energy, Dalian Institute of Chemical Physics, Chinese Academy of Sciences, Dalian 116023, Liaoning, China

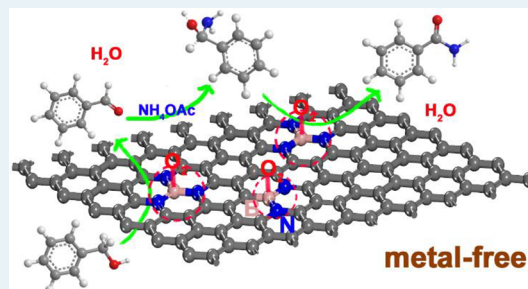
[‡]State Key Laboratory of Catalysis, Dalian Institute of Chemical Physics, Chinese Academy of Sciences, Dalian 116023, Liaoning, China

[§]University of Chinese Academy of Sciences, Beijing 100049, China

^{||}School of Chemistry and Material Science, CAS Center for Excellence in Nanoscience, iChEM, University of Science and Technology of China; Hefei National Laboratory for Physical Sciences at the Microscale, Hefei 230026, China

Supporting Information

ABSTRACT: Metal-free catalysts show environmental friendliness and cost-effectiveness, as well as less susceptibility to poisoning over metal and metal oxide catalysts. In this respect, we present the synthesis and characterization of metal-free mesoporous nitrogen- and boron-codoped nanocarbon (meso-N,B/C), which exhibits good catalytic performance with conversion of 89% and selectivity of 83% toward amide synthesis from primary alcohols using NH₄OAc as an ammonia resource under an oxygen atmosphere. The facile codoping synthetic strategy was executed by pyrolysis of nitrogen-enriched ligand 4,5-diazafluorene-9-one azine (DAA) and H₃BO₃ as a nitrogen and boron content modulator, respectively. Significantly, control experiments revealed that the reaction proceeded through direct oxidative dehydrogenation of hemiaminal after aldehyde-ammonia condensation, which was remarkably different from that in the previous literature. Density functional theory (DFT) calculations further demonstrate that the selective preference for benzamide largely benefits from the strong adsorption and enhanced activity of oxygen molecules via the interaction with a B atom doped in the catalyst. The active sites in the meso-N,B/C catalyst are proposed to be B atom bonded with N within the graphitic carbon sheets. This founding opens up avenues for the development of modified carbon materials on metal-free catalysis.



KEYWORDS: N,B-codoped carbon, mesoporous carbon, primary amides, oxidative dehydrogenation, DFT calculations

INTRODUCTION

Since the past decade, there exists an increasing interest in the development of metal-free catalysts for organic synthesis due to their distinct advantages over metal-based catalysts, such as lower cost as well as higher reliability, biocompatibility, and sustainability.¹ Metal-free materials behave completely differently from traditional metal/metal oxide materials in catalysis, which have revolutionized the field of catalysis.² Carbon materials as typical nonmetallic heterogeneous catalysts have shown promising application on Friedel–Crafts alkylation reactions,³ reductive hydrogen atom transfer reactions,⁴ and oxidation of amines⁵ and arenes.⁶ Heteroatom dopants (e.g., B, N, F, P, or S) can effectively modulate the electrical properties and surface physicochemical features of carbons, resulting in enhanced activity of carbocatalysts or bringing about some new chemical functions.⁷ Specifically, N-doped graphene has been recently found to catalyze selective oxidation of ethylbenzene⁸ and epoxidation of *trans*-stilbene and styrene⁹ owing to the

more metal-like d band electronic structure of the ortho-carbon atom next to the doped N atom. Such a heteroatom doping strategy could tune the electron features of carbon correlated to catalysis. However, reactions are limited to simple catalytic hydrogenations and oxidations currently. Targeting design over the electrical properties of carbocatalysts for other challenging synthetic organic reactions remains a challenge. Finding a practical, effective method to fabricate carbon nanostructures with controllable heteroatom doping may push the limits of metal-free carbocatalyst performance, thus stimulating progress in this area.

Amides and their derivatives represent a commercially important class of compounds given their widespread applications as intermediates for the manufacture of biological

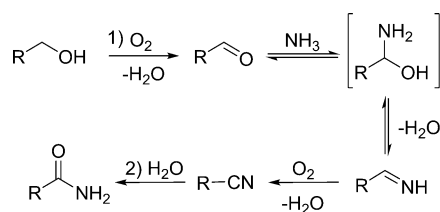
Received: July 23, 2018

Revised: August 29, 2018

Published: September 14, 2018

as well as chemical and polymer compounds.¹⁰ In the drive toward green and sustainable chemistry, direct amide synthesis from readily available alcohol attracts significant interest in which reagents used are nontoxic and pollution-free.¹¹ Since Milstein et al. reported secondary amides synthesis from primary alcohols and amines with a PNN pincer-type Ru complex with evolution of H₂,¹² many successive efforts have been made, and most of them employed noble metals such as homogeneous Ru¹³ and Rh¹⁴ complexes and heterogeneous Ag/ γ -Al₂O₃.¹⁵ In addition, despite the excellent catalytic performance of the heterogeneous Au-based catalysts on amide synthesis from alcohols and amines under molecular oxygen with excessive indispensable base additives,^{16,17} it is hard to implement large-scale application because of exorbitant cost. And when it occurs with inorganic ammonia, applicability of the above-mentioned Au-based system is only limited to benzamide, and the yield is low (50% yield). Recently, a series of primary amides was successfully achieved using Ru(OH)_x/Al₂O₃ in a two-step strategy (Scheme 1):¹⁸

Scheme 1. General Reaction Pathway for Amides Synthesis from Primary Alcohols and Ammonia



(1) Initially, oxidative dehydrogenation of the alcohol to the aldehyde occurs. Condensation of the aldehyde with ammonia proceeds to form a hemiaminal intermediate, followed by dehydration to aldimine, and undergoes immediate oxidative dehydrogenation to nitriles. (2) The nitriles further hydrolyze into the final primary amide product with additional water. Non-noble-metal-based catalysts OMS-2¹⁹ and MnO₂/GO²⁰ have been currently developed for one-step primary amide synthesis from alcohol, which went through the same dehydration–dehydrogenation–hydration sequence as the hemiaminal. In addition, a nanoscale iron oxide catalyst was also occupied to catalyze aromatic aldehyde with ammonia to achieve primary amides.²¹

Despite the significant progress achieved by the above metal-based catalysts, a metal-free catalytic procedure for primary amides still remains strongly desirable from both an economical and ecological perspective, but very challenging. In this contribution, we design and synthesize N,B-codoped nanocarbons via pyrolysis of nitrogen-rich 4,5-diazafluorene-9-one azine (DAA) and H₃BO₃. A hard template method using silica colloid as a template can equip the N,B-codoped nanocarbons with a high specific surface area for preparing a mesoporous codoping nanocarbon meso-N,B/C. The as-designed codoped carbocatalysts show high reactivity toward primary amides directly from primary alcohols using NH₄OAc as an ammonia resource under an oxygen atmosphere. Unexpectedly, the metal-free primary amide synthesis system proceeds via a novel direct oxidative dehydrogenation strategy of the hemiaminal, not the general dehydration–dehydrogenation–hydration sequence reported in the previous literature.

RESULTS AND DISCUSSION

Different mass ratios of polypyridyl ligand DAA and H₃BO₃ as nitrogen and boron resources, respectively, were mixed thoroughly at the molecular level before a SiO₂ nanosphere template was involved. Subsequent pyrolysis at 800 °C for 2 h under a N₂ atmosphere and NaOH etch produced the final meso-N,B/C-*x* (*x* = 3, 1.5, 0.5), where *x* denoted the different mass ratios of DAA and H₃BO₃. For comparison, undoped mesoporous carbon (meso-C) derived from sucrose and bulk N,B/C without any hard template assistant were also prepared. All these materials were tested for their catalytic activity for the benchmark oxidative amidation of benzyl alcohol (**1a**).

As shown in Table 1, the reaction hardly proceeded in the absence of a catalyst (Table 1, entry 1). Precursors DAA and

Table 1. Aerobic Oxidative Amidation of Benzyl Alcohol over Different Catalysts^a

entry	catalyst	conv. (%) ^b	sel. (%) ^b		
			2a	3a	2a/3a
1		8		trace	
2	DAA + H ₃ BO ₃	8		trace	
3	meso-C	26	42	10	4.2
4	meso-N,B/C-3	81	80	11	7.3
5	meso-N,B/C-1.5	89	83	9	9.2
6	meso-N,B/C-0.5	76	84	9	9.3
7	meso-N/C	77	63	18	3.5
8	N,B/C	36	54	13	4.2

^aReaction conditions: **1a** (0.5 mmol), catalyst (50 mg), 2.5 equiv of NH₄OAc, 5 bar of O₂, 1 mL of *t*-amyl alcohol, 130 °C, 18 h.

^bConversion and selectivity were determined by GC, naphthalene as inner standard.

H₃BO₃ were nearly inactive, suggesting that the active species should be formed during pyrolysis (Table 1, entry 2). As expected, undoped mesoporous carbon showed low activity (Table 1, entry 3), whereas the as-designed meso-N,B/C samples obtained by pyrolysis of DAA and H₃BO₃ could considerably prompt the transformation of **1a** under the same conditions (Table 1, entries 4–6). Combining these results with X-ray photoemission spectroscopy (XPS) analysis (Table 2 and S1), it was discovered that when the B concentration increased from 1.52 atom % in the meso-N,B/C-3 sample to 2.36 atom % in the meso-N,B/C-1.5 sample, the selectivity of benzamide (**2a**) versus benzonitrile (**3a**; S_{2a/3a}) was enhanced from 7.3 to 9.2. It seemed that S_{2a/3a} correlated to the doping content of B in consideration of nearly the same N concentration in meso-N,B/C-*x* samples as shown in XPS analysis. However, further multiplying H₃BO₃ dosage only resulted in a slightly greater B concentration (2.67 atom %) in the meso-N,B/C-0.5 sample and, thus, a similar S_{2a/3a} (9.3). The effect of surface area, pore volume, and pore size on the final selectivity should be excluded according to the N₂ physical adsorption analysis results of meso-N,B/C-*x* samples (Table 2). Among them, the meso-N,B/C-1.5 performed the best, giving the highest conversion of **1a** (89%) and selectivity toward **2a** (83%, Table 1, entry 5). For comparison, the meso-N/C catalyst derived solely from DAA was also tested; S_{2a/3a}

Table 2. Textural and Physicochemical Properties of meso-N,B/C-*x*

samples (meso-N,B/C)	S_{BET} (m ² /g)	S_{Micro} (m ² /g)	S_{Meso} (m ² /g)	V_{Total} (cc/g)	D_{pore}^a (nm)	content (%) ^b			
						B	C	N	O
-3	546	177	369	1.41	17.3	1.52	76.93	10.15	11.39
-1.5	513	149	365	1.80	11.9	2.36	77.06	10.11	10.47
-0.5	555	177	378	1.42	12.1	2.67	76.49	10.20	10.63

^aCalculated using the BJH method. ^bMeasured by XPS.

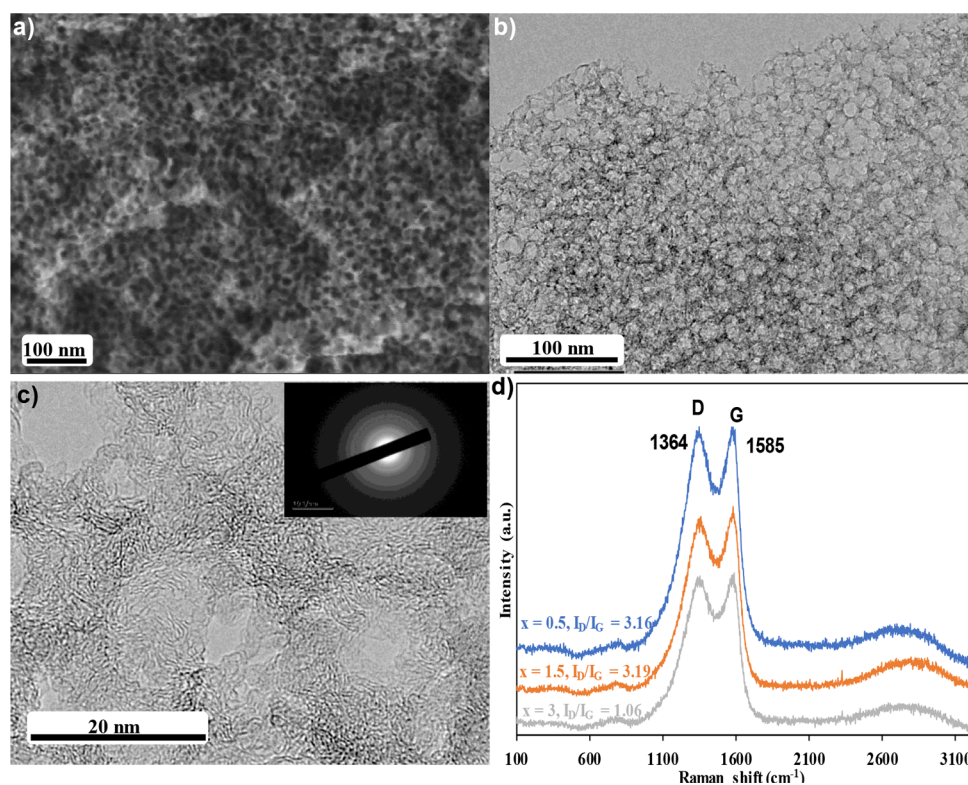


Figure 1. (a) SEM, (b,c) TEM images of meso-N,B/C-1.5, inset: the selected-area electron diffraction (SAED) image. (d) Raman spectrum of meso-N,B/C-*x*.

dropped sharply to 3.5, suggesting that B dopant plays a pivotal role in improving amide selectivity (Table 1, entry 7). The bulk N,B/C catalyst gave low conversion, which indicated that the high surface area and pore volume contribute to exposing more active sites, and thus superior activity (Table 1, entry 8). This conventional concept is corroborated by the fact that the specific surface area increased from 0 to 513 m²/g after the involvement of the SiO₂ template (Table S2). In addition to catalyst optimization, the reaction conditions were also optimized (Tables S3 and S4, Figure S1): 50 mg of meso-N,B/C-1.5, 2.5 equiv of NH₄OAc, 1 mL of *t*-amyl alcohol, reaction temperature at 130 °C under 0.5 MPa of O₂ for 18 h. Considering the relatively low conversion of meso-N,B/C-0.5, we used meso-N,B/C-1.5 as the best-in-class catalyst in all subsequent experiments. All these results indicate the key role of special electronic structure and thus physicochemical properties of carbocatalysts in tuning the reaction chemoselectivity. Moreover, the meso-N,B/C-1.5 catalyst shows good stability after six reactions with a little activity decline (Table S5).

SEM images for as-designed meso-N,B/C were displayed in Figure 1a. The material featured the sponge-like morphology resulting from a silicon sphere template. The interlacing of pores was displayed in TEM images with a diameter of several

to a dozen nanometers (Figure 1b), which is in agreement with N₂ physical adsorption results (Figure S2). At higher resolution, it was observed that the nanocarbon wall was of very high graphitic degree (Figure 1c). As shown in the Raman spectrum, I_D/I_G increased along with the increasing boron doping (1.06 and 3.19 for meso-N,B/C-3 and -1.5), which means higher defect density and disorder degree of nanocarbon material (Figure 1d). The energy-dispersive X-ray (EDX) spectrum clearly proved no metal pollution (Figure S3). Energy-dispersive spectroscopy (EDS) mapping revealed that N and B were uniformly doped into the mesoporous carbon bulk (Figure S4). The uniform doping was due to the molecule-level mixture of DAA and H₃BO₃ before thermal calcination.

To identify the surface chemical state of B and N dopants, we performed XPS on the meso-N,B/C-*x* samples (Figures 2 and S5). The B 1s spectrum could be divided into three components (Figure 2a): the primary binding energy peak of 191.3 eV is assigned to a B–N₃ structure with *h*-BN-like configuration.²² A lower one at 190.5 eV implies a contribution from the B–C bonding configurations in C–B–N₂,²³ which is due to C atoms having a lower electronegativity than N. Another comparable signal at 192.5 eV is characteristic for B–O bonding.^{22c} It is noteworthy that B–C₃ and C₂–B–N should

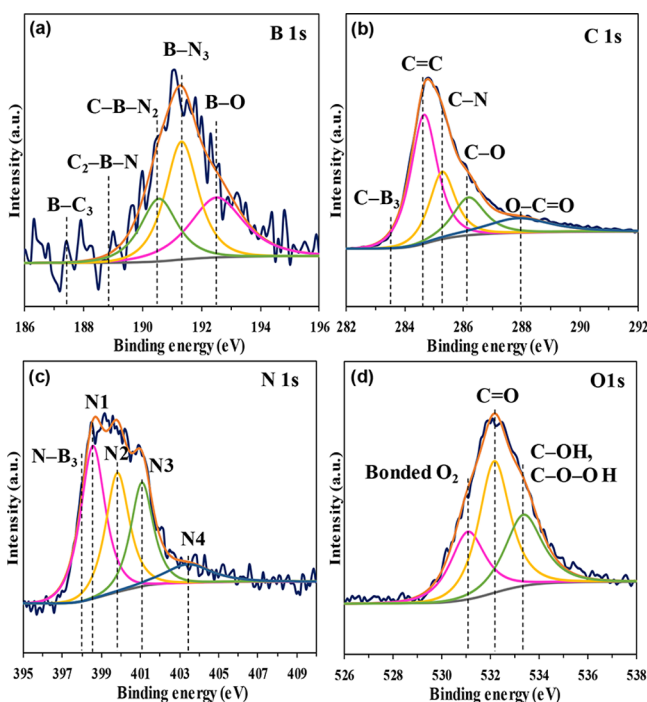


Figure 2. (a) B 1s, (b) C 1s, (c) N 1s, (d) O 1s spectra of meso-N,B/C-1.5.

have a lower binding energy (about 187.4 and 188.9 eV, severally) than C–B–N₂,^{23,24} which has not been observed in all samples. Solid-state ¹¹B MAS NMR spectra have three observable peaks (Figure S6): the broad region at 20–25 ppm signifies a typical *h*-BN structure;²⁵ the sharp peak at 13.3 ppm can be attributed to a B–O structure similar to that of bulk B₂O₃;²⁶ another sharp peak at around 0 ppm results from B–C structure,²⁷ which is consistent with the XPS results. The N 1s spectrum was composed of four peaks centered at 398.6, 399.8, 401.1, and 403.5 eV, corresponding to pyridinic N, pyrrolic N, graphitic N, and pyridinic N-oxide (Figure 2c).²⁸ The main peak at 398.6 eV may include the signal at 398.0 eV from NB₃ trigonal units in *h*-BN.^{22b,d} Combined with the experimental results in Table 1, it was proposed that B bonded with N (B–N₃ or C–B–N₂) was a major active site targeting amides versus nitriles.

In addition, the main C 1s component at 284.7 eV is assigned to graphitic C=C species (Figure 2b), whereas three relatively smaller peaks centered at 285.3, 286.2, and 287.9 eV correspond to different C–N (including B–C–N),²⁴ C–O, and O–C=O bondings.²⁹ The C 1s spectrum revealed that there is scarcely any C–B₃ (283.6 eV) component.^{22a,b} The employment of the inorganic template and the H₃BO₃ precursor resulted unconsciously in a considerable amount of O implant. The O 1s spectrum was deconvoluted into three components with binding energy peaks centering at 533.4, 532.2, and 531.1 eV (Figure 2d). Peaks located at 533.4 and 532.2 eV belonged to the C–OH and/or C–O–O–H groups and C=O groups, respectively. The peak at 531.1 eV corresponds to the absorbed oxygen-containing components (for example, CO₂, H₂O, et al.) According to the literature,^{29a,30} for the sp² carbon material of high surface area, universal strong gas adsorption enables them as catalysts by activating gas, especially polarizable O₂, CO₂, or NO and organic molecules for chemical transformation.

The FTIR spectra of all meso-N,B/C-*x* samples with various contents of boron are shown in Figure 3. Two bands at 772

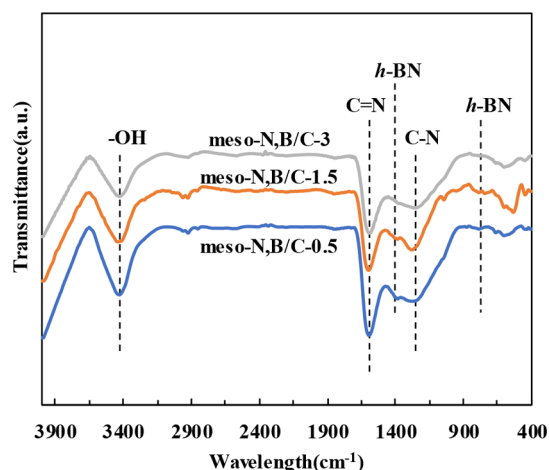


Figure 3. FTIR spectra of meso-N,B/C-*x*.

and 1398 cm⁻¹ are assigned to the characteristic in-plane stretching and out-of-plane bending vibrations of *h*-BN,^{22b,31} respectively, and increased gradually with increasing B content. In agreement with XPS, FTIR demonstrates that boron is involved in the structure of the as-obtained materials and is bonded to N to form a B–N unit. In addition, the broad band at 3430 cm⁻¹ is related to N–H or O–H stretching vibrations or water molecules.³² The stronger bands are assigned to C=N (1590 cm⁻¹) and C–N (1254 cm⁻¹).^{22b} B–O bands (1200, 1350, 1450 cm⁻¹) are overlapping with the carbon–nitrogen bands.

In previous work,^{19,20} it was widely believed that the hemiaminal undergoes a dehydration–dehydrogenation–hydration sequence to amides after aldehyde–ammonia condensation (Figure 4, path B). To figure out whether our system

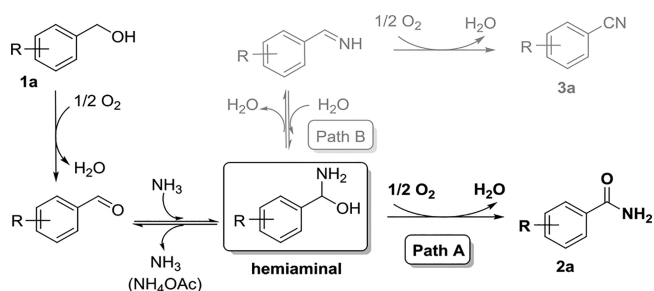
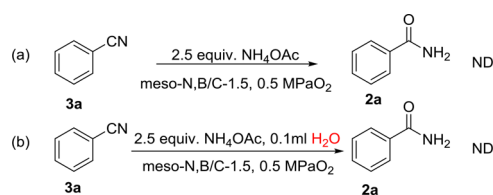


Figure 4. Possible reaction pathway for primary amide synthesis from alcohols.

experienced the hydration of nitriles or not, benzonitrile instead of benzyl alcohol was used as the substrate under standard conditions. It was found that no benzamide was detected, even if water was added (Scheme 2).

On the basis of the results *vide supra*, it is rational to deduce that the present meso-N,B/C-catalyzed system possibly proceeds through the direct challenging oxidative dehydrogenation of hemiaminal (path A). It was indirectly attested that meso-N,B/C was capable of catalyzing the dehydrogenation process by benzaldehyde and tetrahydrofuran reacted to the detectable corresponding amide (Scheme S1).

Scheme 2. Control Experiments



To rationalize the scenario above, BN-doped graphene supercells were built for the density functional theory (DFT) calculations based on the XPS analysis and FTIR spectra (Figure 5a). The optimized adsorption configurations of the

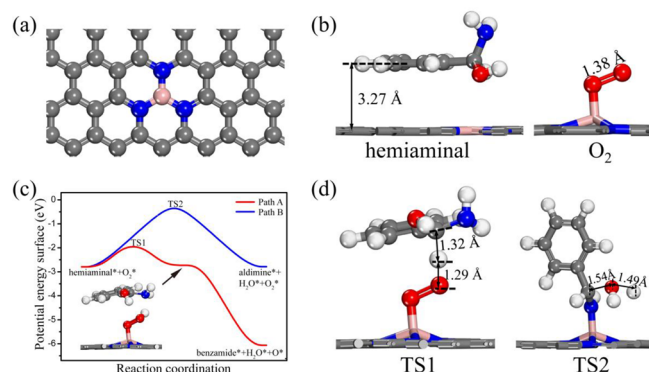


Figure 5. (a) The structure of periodic BN-doped graphene model. (b) The adsorption configurations of hemiaminal (left) and O_2 (right). (c) The potential energy surface of path A and path B. The inset picture shows the corresponding structure of the intermediate, following the dehydrogenation of hemiaminal. (d) Structures of transition states of path A and path B. The gray, blue, pink, and red balls represent carbon, nitrogen, boron, and oxygen atoms, respectively.

hemiaminal and oxygen molecule are shown in Figure 5b, and the corresponding adsorption energies are listed in Table 3. It

Table 3. Adsorption Energetics of Intermediates

intermediates	E_{ads}/eV
hemiaminal	-1.16
O_2	-1.64
OOH	-3.01
H_2O	-0.28
O (w.r.t. $1/2 O_2$)	-2.15
benzamide	-1.11
aldimine	-1.27

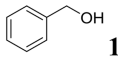
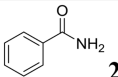
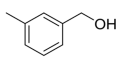
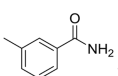
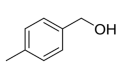
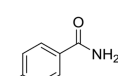
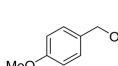
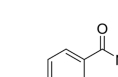
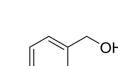
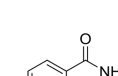
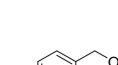
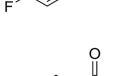

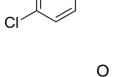
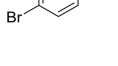
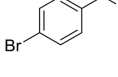
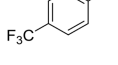
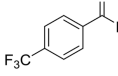
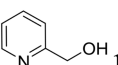
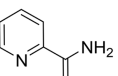
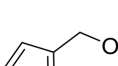
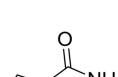
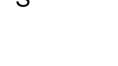
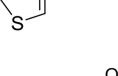
can be found that hemiaminal adsorbs in a parallel manner on the surface, and the benzene ring is about 3.27 Å away from the surface. The calculated adsorption energy is -1.16 eV, mainly due to π - π interaction with respect to the BN-doped graphene. Hemiaminal adsorption in a perpendicular configuration is about 0.45 eV weaker. On the other hand, the calculated adsorption energy of the oxygen molecule is -1.64 eV, stronger binding than hemiaminal. This means that the oxygen molecule rather than hemiaminal will first populate the BN sites, and the adsorbed oxygen molecule at BN sites reacts with the coming hemiaminal afterward. We note that the binding strength of the oxygen molecule toward the BN sites is much stronger than its binding toward the pristine graphene

(-0.21 eV). For graphene doped with graphitic (-0.42 eV) and pyridinic nitrogen (-0.26 eV), though they bind oxygen molecules slightly stronger, subsequent dissociation barrier are as high as 1.70 and 2.14 eV (Figure S7). These results indicate that compared to the pristine graphene or graphene doped with graphitic and pyridinic nitrogen, the B-N sites in graphene are more efficient at adsorbing and activating oxygen molecules.

Potential energy surfaces of path A (oxidative dehydrogenation) and path B (direct dehydration) were calculated and shown in Figure 5c. The adsorption energies of involved intermediates E_{ads} are listed in Table 3. For path A, benzamide is produced via two oxidative dehydrogenation steps. The dehydrogenation of the first hydrogen from the -CH group to an adsorbed oxygen molecule is slightly endothermic with a reaction energy of 0.07 eV and low activation energy of 0.82 eV. The corresponding transition state is given in Figure 5d, TS1. Hemiaminal attacks adsorbed oxygen molecules from the top, and the hydrogen is located in the middle of carbon and oxygen atoms with a bond distance of 1.32 and 1.29 Å, respectively. The modest reaction barrier can be understood via the hydrogen transfer between C and O. For a second dehydrogenation from the -OH group to OOH* to form benzamide and water, the corresponding process is nearly barrierless and highly exothermic with a reaction energy of -3.27 eV. High exothermicity could be rationalized by a strong binding strength between oxygen atoms left with the BN sites, whose dissociative adsorption energy with respect to the oxygen molecule in the gas phase is -2.15 eV (Table 3). As seen from Figure 5c, the overall barrier for two dehydrogenation steps in path A is only 0.82 eV with favorable exothermic reaction energy. In contrast, the barrier for the direct dehydration in path B over the BN site is 2.45 eV with thermal neutral reaction energy. The larger barrier comes mainly from the direct C-O bond breaking and H atom transformation without pronounced stabilization of the corresponding TS (Figure 5d, TS2). Compared to path A, the calculated barrier for direct dehydration (path B) is considerably high, a fact that makes path B kinetically unfavorable. Moreover, as indicated above, the BN sites will be populated mainly by oxygen due to its stronger binding than hemiaminal. In other words, there are actually no sites available for direct dehydration of hemiaminal over the BN sites, a fact that further inhibits path B.

In order to study the scope of the metal-free meso-N,B/C-catalyzed amidation, various kinds of structurally diverse benzylic alcohols were tested, and the desired amides were obtained in moderate to high yields as shown in Table 4. Methylbenzyl alcohol gave toluamides (2b-2c) in moderate yields. In the case of methyl substituted derivatives, the electronic effect resulting from different locations of -CH₃ at the benzene ring was not significant; benzylic alcohols with an electron-donating -OCH₃ group as well as electron-withdrawing halogen substituents can also give about 70% yields of the corresponding primary amides (2d-2g), and it went smoothly without dehalogenation. For strong electron-withdrawing groups, -CF₃ and -NO₂, it also achieved moderate yield of the corresponding primary amides (2h-2i). Furthermore, pyridine and thiophene derivatives could transform to the corresponding amides (2j-2k) in 77% and 54% yields, respectively. Regrettably, it suffered from breakage during the transformation of cinnamyl alcohol, resulting in benzamide being formed as a main product. No adipamide

Table 4. meso-N,B/C-Catalyzed Aerobic Oxidative Amidation of Alcohols to Primary Amides^a

Entry	Substrate	Product	Yield(%)
1	 1a	 2a	74
2	 1b	 2b	55
3	 1c	 2c	64
4	 1d	 2d	72
5	 1e	 2e	61
6	 1f	 2f	67
7	 1g	 2g	73
8	 1h	 2h	50
10	 1j	 2j	77
11	 1k	 2k	54
12	 1l	 2l	16
13	 m	 2m	0

^aReaction conditions: alcohols (0.5 mmol), catalyst (50 mg), NH₄OAc (96 mg, 2.5 equiv), 5 bar O₂, 1 mL of *t*-amyl alcohol, 130 °C, 18 h. Yields were determined by GC and confirmed by GC-MS.

(**2m**) was obtained because of the inactivity of aliphatic alcohols.

CONCLUSION

In summary, a novel nitrogen- and boron-codoped mesoporous carbon of high surface area was successfully prepared through pyrolysis of nitrogen-containing precursors DAA and H₃BO₃ using a hard-template approach. When being used as a metal-free catalyst in the aerobic oxidative amidation of

primary alcohols with NH₄OAc as an ammonia resource under an oxygen atmosphere, the optimal meso-N,B/C-1.5 showed the best catalytic performance with 89% conversion of benzyl alcohol and 83% selectivity for the desired product benzonitrile. Thorough investigations on the surface chemical and physical properties of the material revealed that such a good performance of mesoporous carbon catalysts is ascribed to homogeneous distribution of active B–N units as well as mesoporous structure and high surface area. DFT calculations

further identified the strong interaction of the O₂ molecule with a boron atom in a B–N unit, which further reinforced the activation ability of molecular oxygen. The heteroatom codoping strategy makes the reaction proceed in a direct challenging oxidative dehydrogenation path of hemiaminal, not the general dehydration–dehydrogenation–hydration process. Such an unprecedented example will provide a guide for the development of metal-free catalysts, and expansion toward challenging synthetic organic reactions is underway.

EXPERIMENTAL SECTION

Preparation of Catalysts. DAA was prepared according to the literature (details in the Supporting Information). The typical meso-N₂B/C-*x* catalysts were prepared as follows: DAA and H₃BO₃ (270 mg/90 mg, *x* = 3; 270 mg/180 mg, *x* = 1.5; 270 mg/540 mg, *x* = 0.5) were dissolved in succession into 40 mL of DMF at 130 °C under vigorous stirring. After dissolution, 1200 mg of Ludox HS-40 was added into the mixture under vigorous stirring. After evaporation of the solvent, the obtained DAA/H₃BO₃/SiO₂ composites were directly pyrolyzed under N₂ at a heating ramp rate of 5 °C/min to 800 °C, and the temperature was held for 2 h. Samples resulting from different mass ratios are denoted as meso-N₂B/C-*x* catalysts (*x* = the mass ratio of DAA and H₃BO₃) and finally were obtained after removal of templates by 0.5 M NaOH etching for 5 h at 100 °C. meso-N/C and N₂B/C were prepared in a similar process except for no addition of H₃BO₃ and Ludox HS-40, respectively. meso-C catalyst was derived from sucrose. A total of 1 g of sucrose was added into 40 mL of H₂O under vigorous stirring. Then 1200 mg of Ludox HS-40 was added into the mixture, and then the whole reaction mixture was stirred at 60 °C for 5–6 h. After evaporation of H₂O at 100 °C, the obtained composites made the above pyrolyzation treatment and NaOH-etching process proceed to obtain the as-designed meso-C catalyst.

General Procedure for the Synthesis of Primary Amides and Catalyst Recycling. In a typical amidation, 50 mg of meso-N₂B/C-*x*, 0.5 mmol of benzyl alcohol, 96.4 mg of NH₄OAc (2.5 equiv with respect to benzyl alcohol), and 1 mL of *t*-amyl alcohol were placed in a vial fitted with a magnetic stir bar, septum, cap, and needle. The vial was attached inside an autoclave, and the reaction was carried out at 130 °C in O₂ (5 atm). Subsequently, the autoclave was stirred at the required time. After the completion of the reaction, the vials were removed from the autoclave. Naphthalene as a standard was added, and the reaction product was diluted with tetrahydrofuran followed by centrifugation and then analyzed by GC and GC mass spectrometry (GC-MS). The meso-N₂B/C catalyst was separated by filtration, washed with methanol, and then calcined at 800 °C in N₂ prior to its use in the reuse experiment.

Catalyst Characterization. Nitrogen sorption isotherms were determined at –196 °C using a QuadraSorb SI4 Station. Prior to the measurement, the samples were degassed in a vacuum at 300 °C for 3 h, and the Brunauer–Emmett–Teller (BET) surface areas of the samples were calculated using adsorption data. X-ray photoelectron spectroscopy (XPS) measurement was performed with an ESCALAB 250Xi imaging photoelectron spectrometer (Thermo Fisher Scientific, USA) using a monochromatic Al K α X-ray ($h\nu = 1846.6$ eV). Energy calibration was carried out using the C 1s peak of adventitious C at 284.8 eV. Transmission electron microscope

(TEM) characterization was conducted on a JEM-2100 microscope. Scanning electron microscope (SEM) images were conducted on a JSM-7800F microscope operating at an acceleration voltage of 20 kV.

Computational Details. A p(3 × 5) monolayer of graphene slab, where a BN₃ unit substitutes four carbon atoms, was used to model the corresponding adsorption and reaction. All spin polarized DFT calculations were performed with the Vienna ab initio simulation package (VASP).³³ In order to capture the van der Waal interactions between molecules and the substrate, nonlocal functional optB86b-vdW was used.³⁴ Kohn–Sham orbitals were extended in a plane wave basis with a cutoff energy of 400 eV.

The substrate and adsorption molecules were fully relaxed during the calculation. A vacuum level of 20 Å was sufficient to avoid interactions between periodic slabs. The convergence energy and force were set to 1 × 10^{–4} eV and 0.02 eV/Å, respectively. Transition states (TSs) were determined by climbing-image nudged elastic band (CI-NEB) methods³⁵ and confirmed by frequency analysis.

The adsorption energy E_{ads} and activation energy of transition state E_{act} were calculated as

$$E_{\text{ads}} = E_{\text{ads/sub}} - E_{\text{mol}} - E_{\text{sub}} \quad (1)$$

$$E_{\text{act}} = (E_{\text{act/sub}} + E_{\text{sub}}) - (E_{\text{ads1/sub}} + E_{\text{ads2/sub}}) \quad (2)$$

The $E_{\text{ads/sub}}$, E_{mol} , E_{sub} , $E_{\text{act/sub}}$, $E_{\text{ads1/sub}}$, and $E_{\text{ads2/sub}}$ are the total energy of the adsorbed molecule, molecule in the gas phase, the pure slab, the transition state, and adsorbed molecules which are the reactants to form the transition state, respectively.

ASSOCIATED CONTENT

Supporting Information

The Supporting Information is available free of charge on the ACS Publications website at DOI: 10.1021/acscatal.8b02889.

Synthesis of DAA, optimization of reaction conditions, N₂ adsorption analysis, XPS, EDX, elemental maps, ¹¹B NMR, control experiments (PDF)

AUTHOR INFORMATION

Corresponding Authors

*E-mail: sgao@dicp.ac.cn.

*E-mail: wxli70@ustc.edu.cn.

ORCID

Wei-Xue Li: 0000-0002-5043-3088

Shuang Gao: 0000-0002-6875-9166

Author Contributions

[†]Sensen Shang and Pei-Pei Chen contributed equally.

Notes

The authors declare no competing financial interest.

ACKNOWLEDGMENTS

We gratefully acknowledge the support of the National Natural Science Foundation of China (21773232, 21773227, 91645202), the Frontier Science Key Project of the Chinese Academy of Sciences (QYZDJ-SSW-SLH054), and the National Key R&D Program of China (2017YFB0602205, 2018YFA0208603).

REFERENCES

- (1) Fang, Y.; Wang, X. Metal-Free Boron-Containing Heterogeneous Catalysts. *Angew. Chem., Int. Ed.* **2017**, *56*, 15506–15518.
- (2) (a) Su, C.; Acik, M.; Takai, K.; Lu, J.; Hao, S.-j.; Zheng, Y.; Wu, P.; Bao, Q.; Enoki, T.; Chabal, Y. J.; Ping Loh, K. Probing the catalytic activity of porous graphene oxide and the origin of this behaviour. *Nat. Commun.* **2012**, *3*, 1298. (b) Su, D. S.; Perathoner, S.; Centi, G. Nanocarbons for the Development of Advanced Catalysts. *Chem. Rev.* **2013**, *113*, 5782–5816.
- (3) Hu, F.; Patel, M.; Luo, F.; Flach, C.; Mendelsohn, R.; Garfunkel, E.; He, H.; Szostak, M. Graphene-Catalyzed Direct Friedel–Crafts Alkylation Reactions: Mechanism, Selectivity, and Synthetic Utility. *J. Am. Chem. Soc.* **2015**, *137*, 14473–14480.
- (4) Yang, H.; Cui, X.; Dai, X.; Deng, Y.; Shi, F. Carbon-catalyzed reductive hydrogen atom transfer reactions. *Nat. Commun.* **2015**, *6*, 6478.
- (5) Huang, H.; Huang, J.; Liu, Y.-M.; He, H.-Y.; Cao, Y.; Fan, K.-N. Graphite oxide as an efficient and durable metal-free catalyst for aerobic oxidative coupling of amines to imines. *Green Chem.* **2012**, *14*, 930–934.
- (6) (a) Yang, J.-H.; Sun, G.; Gao, Y.; Zhao, H.; Tang, P.; Tan, J.; Lu, A.-H.; Ma, D. Direct catalytic oxidation of benzene to phenol over metal-free graphene-based catalyst. *Energy Environ. Sci.* **2013**, *6*, 793–798. (b) Wen, G.; Wu, S.; Li, B.; Dai, C.; Su, D. S. Active Sites and Mechanisms for Direct Oxidation of Benzene to Phenol over Carbon Catalysts. *Angew. Chem., Int. Ed.* **2015**, *54*, 4105–4109.
- (7) (a) Long, J.; Xie, X.; Xu, J.; Gu, Q.; Chen, L.; Wang, X. Nitrogen-doped graphene nanosheets as metal-free catalysts for aerobic selective oxidation of benzylic alcohols. *ACS Catal.* **2012**, *2*, 622–631. (b) Kong, X.-k.; Sun, Z.-y.; Chen, M.; Chen, C.-l.; Chen, Q.-w. Metal-free catalytic reduction of 4-nitrophenol to 4-aminophenol by N-doped graphene. *Energy Environ. Sci.* **2013**, *6*, 3260–3266. (c) Guo, F.; Yang, P.; Pan, Z.; Cao, X.-N.; Xie, Z.; Wang, X. Carbon-Doped BN Nanosheets for the Oxidative Dehydrogenation of Ethylbenzene. *Angew. Chem.* **2017**, *129*, 8343–8347. (d) Huang, B.; Peng, L.; Yang, F.; Liu, Y.; Xie, Z. Improving ORR activity of carbon nanotubes by hydrothermal carbon deposition method. *J. Energy Chem.* **2017**, *26*, 712–718.
- (8) Gao, Y.; Hu, G.; Zhong, J.; Shi, Z.; Zhu, Y.; Su, D. S.; Wang, J.; Bao, X.; Ma, D. Nitrogen-Doped sp²-Hybridized Carbon as a Superior Catalyst for Selective Oxidation. *Angew. Chem., Int. Ed.* **2013**, *52*, 2109–2113.
- (9) Li, W.; Gao, Y.; Chen, W.; Tang, P.; Li, W.; Shi, Z.; Su, D.; Wang, J.; Ma, D. Catalytic Epoxidation Reaction over N-Containing sp² Carbon Catalysts. *ACS Catal.* **2014**, *4*, 1261–1266.
- (10) Maberlmann, C. E. In *Encyclopedia of Chemical Technology*; Kroschwitz, J. I., Ed.; Wiley: New York, 1991; Vol. 1, pp 251–266.
- (11) (a) Smith, M. B. In *Organic Synthesis*, 2nd ed.; Mc-Graw-Hill Companies: New York, 2002. (b) Valeur, E.; Bradley, M. Amide bond formation: beyond the myth of coupling reagents. *Chem. Soc. Rev.* **2009**, *38*, 606–631.
- (12) Gunanathan, C.; Ben-David, Y.; Milstein, D. Direct Synthesis of Amides from Alcohols and Amines with Liberation of H₂. *Science* **2007**, *317*, 790–792.
- (13) (a) Zeng, H.; Guan, Z. Direct Synthesis of Polyamides via Catalytic Dehydrogenation of Diols and Diamines. *J. Am. Chem. Soc.* **2011**, *133*, 1159–1161. (b) Dam, J. H.; Osztrovsky, G.; Nordstrom, L. U.; Madsen, R. Amide Synthesis from Alcohols and Amines Catalyzed by Ruthenium N-Heterocyclic Carbene Complexes. *Chem. - Eur. J.* **2010**, *16*, 6820–6827. (c) Zhang, J.; Senthikumar, M.; Ghosh, S. C.; Hong, S. H. Synthesis of Cyclic Imides from Simple Diols. *Angew. Chem., Int. Ed.* **2010**, *49*, 6391–6395. (d) Watson, A. J. A.; Maxwell, A. C.; Williams, J. M. J. Ruthenium-Catalyzed Oxidation of Alcohols into Amides. *Org. Lett.* **2009**, *11*, 2667–2670. (e) Ghosh, S. C.; Muthaiah, S.; Zhang, Y.; Xu, X.; Hong, S. H. Direct Amide Synthesis from Alcohols and Amines by Phosphine-Free Ruthenium Catalyst Systems. *Adv. Synth. Catal.* **2009**, *351*, 2643–2649. (f) Nordström, L. U.; Vogt, H.; Madsen, R. Amide Synthesis from Alcohols and Amines by the Extrusion of Dihydrogen. *J. Am. Chem. Soc.* **2008**, *130*, 17672–17673.
- (14) Zweifel, T.; Naubron, J.-V.; Grützmacher, H. Catalyzed Dehydrogenative Coupling of Primary Alcohols with Water, Methanol, or Amines. *Angew. Chem., Int. Ed.* **2009**, *48*, 559–563.
- (15) Shimizu, K.-i.; Ohshima, K.; Satsuma, A. Direct Dehydrogenative Amide Synthesis from Alcohols and Amines Catalyzed by γ -Alumina Supported Silver Cluster. *Chem. - Eur. J.* **2009**, *15*, 9977–9980.
- (16) Wang, Y.; Zhu, D.; Tang, L.; Wang, S.; Wang, Z. Highly Efficient Amide Synthesis from Alcohols and Amines by Virtue of a Water-Soluble Gold/DNA Catalyst. *Angew. Chem., Int. Ed.* **2011**, *50*, 8917–8921.
- (17) Soulé, J.-F. o.; Miyamura, H.; Kobayashi, S. Powerful amide synthesis from alcohols and amines under aerobic conditions catalyzed by gold or gold/iron-nickel or-cobalt nanoparticles. *J. Am. Chem. Soc.* **2011**, *133*, 18550–18553.
- (18) Oishi, T.; Yamaguchi, K.; Mizuno, N. Catalytic oxidative synthesis of nitriles directly from primary alcohols and ammonia. *Angew. Chem.* **2009**, *121*, 6404–6406.
- (19) (a) Yamaguchi, K.; Kobayashi, H.; Wang, Y.; Oishi, T.; Ogasawara, Y.; Mizuno, N. Green oxidative synthesis of primary amides from primary alcohols or aldehydes catalyzed by a cryptomelane-type manganese oxide-based octahedral molecular sieve, OMS-2. *Catal. Sci. Technol.* **2013**, *3*, 318–327. (b) Yamaguchi, K.; Kobayashi, H.; Oishi, T.; Mizuno, N. Heterogeneously catalyzed synthesis of primary amides directly from primary alcohols and aqueous ammonia. *Angew. Chem.* **2012**, *124*, 559–562.
- (20) Nie, R.; Shi, J.; Xia, S.; Shen, L.; Chen, P.; Hou, Z.; Xiao, F.-S. MnO₂/graphene oxide: a highly active catalyst for amide synthesis from alcohols and ammonia in aqueous media. *J. Mater. Chem.* **2012**, *22*, 18115–18118.
- (21) Murugesan, K.; Senthamarai, T.; Sohail, M.; Sharif, M.; Kalevaru, N. V.; Jagadeesh, R. V. Stable and reusable nanoscale Fe₂O₃-catalyzed aerobic oxidation process for the selective synthesis of nitriles and primary amides. *Green Chem.* **2018**, *20*, 266–273.
- (22) (a) Ci, L.; Song, L.; Jin, C.; Jariwala, D.; Wu, D.; Li, Y.; Srivastava, A.; Wang, Z.; Storr, K.; Balicas, L.; Liu, F.; Ajayan, P. M. Atomic layers of hybridized boron nitride and graphene domains. *Nat. Mater.* **2010**, *9*, 430. (b) Lei, W.; Portehault, D.; Dimova, R.; Antonietti, M. Boron Carbon Nitride Nanostructures from Salt Melts: Tunable Water-Soluble Phosphors. *J. Am. Chem. Soc.* **2011**, *133*, 7121–7127. (c) Prakash, A.; Sundaram, K. B. Optical and XPS studies of BCN thin films by co-sputtering of B₄C and BN targets. *Appl. Surf. Sci.* **2017**, *396*, 484–491. (d) Miyamoto, Y.; Rubio, A.; Cohen, M. L.; Louie, S. G. Chiral tubules of hexagonal BC₂N. *Phys. Rev. B: Condens. Matter Mater. Phys.* **1994**, *50*, 4976–4979.
- (23) Tabassum, H.; Zou, R.; Mahmood, A.; Liang, Z.; Guo, S. A catalyst-free synthesis of B, N co-doped graphene nanostructures with tunable dimensions as highly efficient metal free dual electrocatalysts. *J. Mater. Chem. A* **2016**, *4*, 16469–16475.
- (24) Beniwal, S.; Hooper, J.; Miller, D. P.; Costa, P. S.; Chen, G.; Liu, S.-Y.; Dowben, P. A.; Sykes, E. C. H.; Zurek, E.; Enders, A. Graphene-like Boron–Carbon–Nitrogen Monolayers. *ACS Nano* **2017**, *11*, 2486–2493.
- (25) Murakami, M.; Shimizu, T.; Tansho, M.; Vinu, A.; Ariga, K.; Takegoshi, K. Chemically nonequivalent sites in mesoporous BCN revealed by solid-state NMR at 21.8 T. *Chem. Lett.* **2006**, *35*, 986–987.
- (26) Zielniok, D.; Cramer, C.; Eckert, H. Structure/Property Correlations in Ion-Conducting Mixed-Network Former Glasses: Solid-State NMR Studies of the System Na₂O–B₂O₃–P₂O₅. *Chem. Mater.* **2007**, *19*, 3162–3170.
- (27) Andreev, Y. G.; Lundström, T.; Harris, R. K.; Oh, S.-W.; Apperley, D. C.; Thompson, D. P. On the nature of boron-carbon-nitrogen compounds synthesised from organic precursors. *J. Alloys Compd.* **1995**, *227*, 102–108.
- (28) (a) Koslowski, U.; Herrmann, I.; Bogdanoff, P.; Barkschat, C.; Fiechter, S.; Iwata, N.; Takahashi, H.; Nishikori, H. Evaluation and

Analysis of PEM-FC Performance using Non-Platinum Cathode Catalysts based on Pyrolysed Fe-and Co-Porphyrins-Influence of a Secondary Heat-treatment. *ECS Trans* **2008**, *13*, 125–141. (b) Wu, G.; Johnston, C. M.; Mack, N. H.; Artyushkova, K.; Ferrandon, M.; Nelson, M.; Lezama-Pacheco, J. S.; Conradson, S. D.; More, K. L.; Myers, D. J.; Zelenay, P. Synthesis-structure-performance correlation for polyaniline-Me-C non-precious metal cathode catalysts for oxygen reduction in fuel cells. *J. Mater. Chem.* **2011**, *21*, 11392–11405.

(29) (a) He, W.; Jiang, C.; Wang, J.; Lu, L. High-Rate Oxygen Electroreduction over Graphitic-N Species Exposed on 3D Hierarchically Porous Nitrogen-Doped Carbons. *Angew. Chem., Int. Ed.* **2014**, *53*, 9503–9507. (b) Li, D.; Chen, Y.; Zheng, M.; Zhao, H.; Zhao, Y.; Sun, Z. Hierarchically Structured Porous Nitrogen-Doped Carbon for Highly Selective CO₂ Capture. *ACS Sustainable Chem. Eng.* **2016**, *4*, 298–304.

(30) Datsyuk, V.; Kalyva, M.; Papagelis, K.; Parthenios, J.; Tasis, D.; Siokou, A.; Kallitsis, I.; Galiotis, C. Chemical oxidation of multiwalled carbon nanotubes. *Carbon* **2008**, *46*, 833–840.

(31) Geick, R.; Perry, C. H.; Rupprecht, G. Normal Modes in Hexagonal Boron Nitride. *Phys. Rev.* **1966**, *146*, 543–547.

(32) Portehault, D.; Giordano, C.; Gervais, C.; Senkowska, I.; Kaskel, S.; Sanchez, C.; Antonietti, M. High-Surface-Area Nanoporous Boron Carbon Nitrides for Hydrogen Storage. *Adv. Funct. Mater.* **2010**, *20*, 1827–1833.

(33) (a) Kresse, G.; Furthmüller, J. Efficiency of ab-initio total energy calculations for metals and semiconductors using a plane-wave basis set. *Comput. Mater. Sci.* **1996**, *6*, 15–50. (b) Kresse, G.; Furthmüller, J. Efficient iterative schemes for ab initio total-energy calculations using a plane-wave basis set. *Phys. Rev. B: Condens. Matter Mater. Phys.* **1996**, *54*, 11169–11186.

(34) Klimeš, J.; Bowler, D. R.; Michaelides, A. Van der Waals density functionals applied to solids. *Phys. Rev. B: Condens. Matter Mater. Phys.* **2011**, *83*, 195131.

(35) (a) Henkelman, G.; Uberuaga, B. P.; Jónsson, H. A climbing image nudged elastic band method for finding saddle points and minimum energy paths. *J. Chem. Phys.* **2000**, *113*, 9901–9904. (b) Henkelman, G.; Jónsson, H. Improved tangent estimate in the nudged elastic band method for finding minimum energy paths and saddle points. *J. Chem. Phys.* **2000**, *113*, 9978–9985.